



High photocatalytic performance of bismuth phosphate and corresponding photodegradation mechanism of Rhodamine B

A. Bouddouch^{1,2} · E. Amaterz¹ · B. Bakiz¹ · F. Guinneton² · A. Taoufyq¹ · S. Villain² · J.-R. Gavarri² · M. Mansori³ · J.-C. Valmalette² · A. Benlhachemi¹

Received: 6 April 2022 / Accepted: 1 June 2022 / Published online: 17 June 2022
© The Author(s), under exclusive licence to Springer Nature B.V. 2022

Abstract

Submicronic BiPO₄ particles (BiP), synthesized via solid-state reaction process at 500 °C, have shown high-performing photocatalytic activity towards Rhodamine B (RhB) degradation under UV irradiation. To better evidence these observed high performances, other commercial particles of TiO₂, ZnO, and Bi₂O₃ were used for comparisons. X-ray diffraction (XRD) was used to characterize all polycrystalline phases. The as-synthesized BiP was single phase crystallizing in a monoclinic structure with space group P2₁/n. The scanning electron microscopy (SEM) analyses of all samples allowed comparing the different average crystallite sizes. The photodegradation of RhB aqueous solution was studied as a function of time, successively in presence of the BiP, TiO₂, ZnO, and Bi₂O₃ photocatalysts. The well-crystallized submicron BiP particles exhibit the highest apparent rate constants compared to commercial materials. The observed photoluminescence emission of these BiP particles under UV excitation can be attributed to specific surface defects. The photocatalytic degradation mechanism of RhB has been proposed in detail using a variety of analytical techniques.

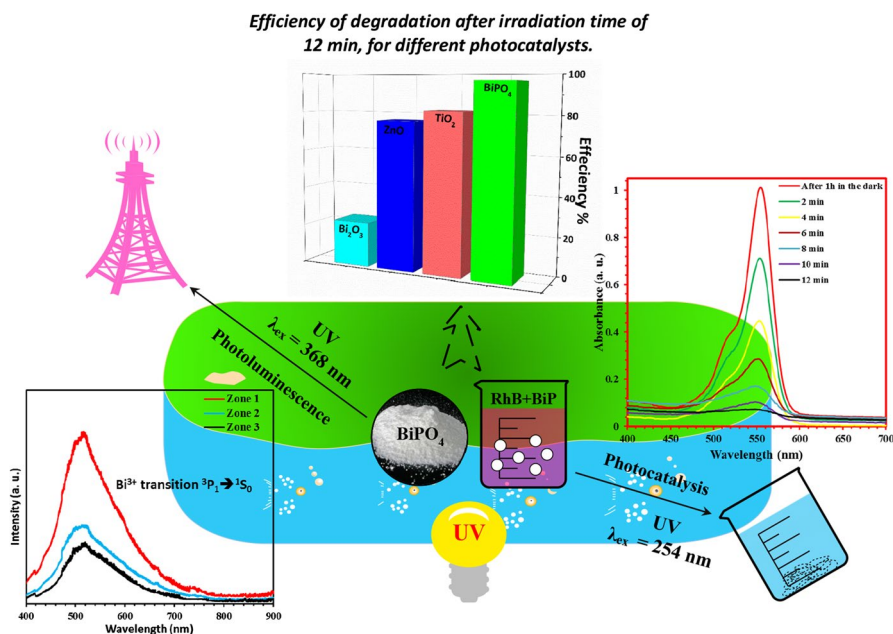
✉ A. Bouddouch
abdo.bouddouch@gmail.com

¹ Laboratoire Matériaux et Environnement (LME), Faculté des Sciences, Université Ibn Zohr, Cité Dakhla, B.P 8106, Agadir, Morocco

² Université de Toulon, Aix Marseille Univ., CNRS 7334, IM2NP, BP 20132, 83957 La Garde Cedex, France

³ IMED-Lab, Faculty of Sciences and Technology, University Cadi Ayyad (UCA), Bd. Abdelkrim El Khattabi, PB 618, Guéliz, 40100 Marrakesh, Morocco

Graphical abstract



Keywords Monoclinic BiPO₄ · Solid-state reaction · Photocatalysis · Photoluminescence · Rhodamine B · Photodegradation mechanism

Introduction

In the general framework of water depollution [1–7], phosphate-based photocatalysts were considered in the literature [8–15] as interesting photocatalysts susceptible to oxidize various pollutants such as RhB or methylene blue [16, 17]. Among these materials, bismuth phosphate (BiPO₄ noted as BiP) can be used as photocatalytic and/or photoluminescent material. The BiP can crystallize in three polymorphic forms: low-temperature hexagonal phase (H, space group: P3₁21), monoclinic phase (M₁, space group: P2₁/n), and monoclinic phase (M₂, space group: P2₁/m) [18]. The M₁ phase shows the highest photocatalytic activity compared with one of the other polymorphs [10]. It should be noted that this M₁ phase is characterized by a wide band gap energy (3.85 eV) [19, 20].

To improve the photocatalytic and/or photoluminescent properties [21–23], various strategies have been developed, including (i) the formation of crystal defects [24–29], (ii) the formation of heterojunctions [30–35], (iii) the broadening of the absorption range and modification of band gaps by doping with active elements [36–41], (iv) the change in synthesis method [42–45]. Among these different strategies, the presence of defects (i) is an important factor in designing photocatalysts

and improving their properties. This was observed in our previous study [24] on BiPO_4 polymorphs obtained from thermal decomposition of precursor hydrate $\text{BiPO}_4 \cdot x\text{H}_2\text{O}$ synthesized by a coprecipitation route. Variable photocatalytic properties were obtained from different mix systems of BiPO_4 polymorphs resulting from thermal treatments at various temperatures. Depending on the temperature of thermal decomposition, a biphasic system was observed: $(\text{H} + \text{M}_1)$ or $(\text{M}_1 + \text{M}_2)$ at intermediate temperatures, and M_2 at high temperature. In this previous study, we concluded that the optimization of photocatalytic efficiency could be ascribed to thermal decomposition favoring the formation of surface structural defects. Photoluminescence experiments under UV excitation (364 nm) revealed large emissions bands for all polymorphs. A 510 nm spectral component corresponded to a mix system $(\text{H} + \text{M}_1)$, and a doublet (520 nm + 650 nm) corresponded to the M_2 monoclinic form. These emissions were ascribed to defects (e.g. bismuth and oxygen vacancies) generated by the thermal decomposition process. The role of defects was also responsible for emissions in the case of $\text{Mn}_3(\text{PO}_4)_2$ [46] characterized by green or red emissions. In the case of SmPO_4 [47], strong photoluminescent emissions were observed in the orange–red color range.

In the present work, we focused on the synthesis of polycrystalline BiPO_4 by solid-state reaction and avoiding biphasic systems, thus obtaining the single M_1 monoclinic phase. RhB was chosen to simulate a general dye pollutant. The photocatalytic activity in presence of RhB of this BiPO_4 photocatalyst is compared to the ones of the TiO_2 , ZnO , and Bi_2O_3 commercial catalysts. Using different techniques (UV–Visible spectrometry, high-performance liquid chromatography (HPLC- UV/Vis) and liquid chromatography coupled to tandem Mass Spectrometry (LC- MS/MS), we proposed a mechanism of degradation of the RhB over these BiP (M_1) photocatalytic particles.

Experimental section

Reagents

Titanium oxide ($\text{TiO}_2 \geq 99.5\%$) and bismuth oxide ($\text{Bi}_2\text{O}_3 \geq 99.9\%$) were purchased from Fluka Chemika. Ammonium hydrogen phosphate ($(\text{NH}_4)\text{H}_2\text{PO}_4 \geq 98.0\%$) was purchased from ProLabo. Zinc oxide ($\text{ZnO} \geq 99.9\%$) was purchased from Aldrich. The azo dye (Rhodamine B) used in this work was obtained from Sigma-Aldrich. The purity of the dye was greater than 95%. The commercial TiO_2 , ZnO , and Bi_2O_3 powders will be used as standard photocatalysts in our photodegradation experiments. All the Reagents were used as received without further purification.

Preparation of BiPO_4 particles

Presently, solid-state reaction was used to prepare BiPO_4 bismuth phosphate from the two commercial bismuth oxide Bi_2O_3 and ammonium hydrogen phosphate $(\text{NH}_4)\text{H}_2\text{PO}_4$. Suitable amounts of these starting precursors were ground in an agate

mortar and then thermally treated at 500 °C for 3 h. The choice of this temperature resulted from our previous work [48] on BiPO₄.

Characterizations

The crystalline powder identification was carried out using X-ray diffraction (XRD). The XRD patterns of the different polycrystalline samples were recorded at room temperature using an Empyrean Panalytical diffractometer operating at 45 kV/35 mA, using the Cu-K(α_1 – α_2) radiation ($\lambda = 1.5406$ and 1.5444 Å) of copper source with Ni filter, and working in continuous mode with a step size of 0.003° .

Scanning electron microscopy (SEM) analysis allowed observing the morphologies and determining the crystallite sizes of all samples, including the commercial standards (TiO₂, ZnO, Bi₂O₃). The device used was a Supra 40 VP Column Gemini Zeiss, operated at 20 keV, coupled with an Energy Dispersive X-rays Spectroscopy (EDXS) type analyzer, allowing determining the local chemical composition of our materials.

Raman spectroscopy allowed correlating the vibrational characteristics of BiPO₄ phase with the XRD structural analyses. The spectrometer Horiba Jobin–Yvon HR800 LabRam system, with wavenumbers of Raman shifts ranging between 100 and 1500 cm⁻¹, was used to register the Raman spectra at room temperature. The excitation source was a 633 nm line of a He–Ne laser; the photonic power applied to the samples was limited to 5 μW with an acquisition time of 5 s.

Photocatalytic experiments

The photocatalytic (PC) reactor used in this work consisted of a light source of 5 UV lamps (Puritec lamp, HNS S 7W, $\lambda = 254$ nm). The solution to be irradiated was placed in a beaker, in the middle of our reactor, in which its homogeneity was ensured by a magnetic stirrer. A cooling system was adopted to avoid any temperature effect. The aqueous solution temperature was maintained between 26 and 28 °C.

The performances of the different photocatalysts were evaluated through the photocatalytic degradation of RhB. Each polycrystalline photocatalyst (fixed mass of 100 mg) was suspended in 100 mL of an aqueous solution of RhB with a concentration of 5 mg L⁻¹. Before irradiation, the solution was stirred for 1 h inside the reactor to get the adsorption–desorption equilibrium between the support and RhB. During irradiation, 3 mL aliquots were collected at time intervals of 2 min. UV visible JENWAY-6705 spectrometry was used to determine the concentration of RhB as a function of irradiation time t . In the case of low concentrations of pollutant, the time-dependent degradation efficiency $DE(t)$ in % can be described by the following Eq. (1):

$$DE(t) = 100 \cdot (I_0 - I(t)) / I_0 = 100 \cdot (1 - C(t) / C_0) \quad (1)$$

where I_0 is the initial absorbance intensity at $t = 0$, proportional to the initial concentration C_0 of RhB, and $I(t)$ is the absorbance intensity at time t , proportional to the

concentration $C(t)$ at time t . The time-dependent $C(t)$ can obey a pseudo-first order kinetics law with the relations:

$$-dC(t)/dt = k \cdot C(t) \quad (2a)$$

$$\text{or } Ln[C_0/C(t)] = k \cdot t \quad (2b)$$

where k is the apparent kinetics constant characteristic of the photocatalyst. It should be noted that this apparent kinetics constant depends on the nature of crystallite surfaces, typically of surface defects, and depend on the total particle surfaces exposed to irradiation.

Product analysis and identification using LC-UV/Vis-MS studies

The standard solutions of the pollutants studied in this work and the intermediates generated in the photo-oxidative process were analyzed with a TSQ Endura TQH-E1-0557 liquid chromatograph, equipped with a diode array detector (multiple wavelengths) and with a column C18. The separation by HPLC was carried out using a mixed eluent of methanol and water ($\text{CH}_3\text{OH}:\text{H}_2\text{O}=2:1$ by volume) and with a flow rate of 1 mL min^{-1} . The degradation products of RhB were also analyzed by the SM-ESI technique in positive ion mode.

The analysis conditions were typically as follows:

- Type of ionization source: H-ESI; ion polarity mode: positive ion mode; capillary voltage: 3.5 kV; sheath gas flow rate (nitrogen): 35 L min^{-1} ; auxiliary gas flow: 5 L min^{-1} ; type of sweep: full sweep; mass range: 50–700 m/z.

Photoluminescence experiments

To perform photoluminescence (PL) tests under UV excitation, Horiba Jobin–Yvon HR800 LabRam spectrometer, equipped with an argon ionized laser as an excitation source with a wavelength of 364.8 nm (3.4 eV), and a power fixed at $5 \mu\text{W}$, was used. The entrance slit, positioned behind the filter, is a diaphragm with a diameter variable between 50 to 500 μm . The exposed polycrystalline sample is obtained by compression on a glass slide. 1 mm in diameter irradiated zone was limited for all samples. The spherical mirror, characterized by an 800 mm focal length, allows revealing the scattered radiation from the input to the dispersive grating to obtain a spectra slot. The measurements were recorded in the spectral range between 400 and 900 nm with an acquisition time of 5 s.

Results and discussion

X-ray diffraction

The X-ray diffraction pattern of bismuth phosphate is shown in Fig. 1. The diffraction pattern corresponds to the JCPDS file 01-089-0289 (High-score software) characteristic of the monoclinic phase $P2_1/n$ (M_1). A simple analysis of the separation of the doublet $K\alpha_1$ – $K\alpha_2$ of Bragg peaks at high 2θ angles clearly shows the high degree of crystallization of this BiP powder. No trace of other phase was detected. The XRD pattern of the standard TiO_2 (Figure SI.1a) shows the sole presence of anatase phase with tetragonal structure (Space group: $I4_1/a$ m d, JCPDS 03-065-5714). The XRD pattern of ZnO (Figure SI.1b) shows a single phase with hexagonal structure (Space group: $P6_3m$ c, JCPDS 03-065-3411). For the Bi_2O_3 powder, the XRD pattern (Figure SI.1c) is characteristic of a single phase with monoclinic structure (Space group: $P2_1/c$, JCPDS 01-071-2274).

Microstructural study by scanning electron microscopy (SEM)

The bismuth phosphate powder morphologies are illustrated in Fig. 2a. The EDS microanalysis presented in Fig. 2b was performed on several areas of the $BiPO_4$ surface to determine their compositions. It showed the presence of the following elements Bi, P, and O with atomic percentages 51.3% and 48.7% for Bi and P respectively (Table 1), with a molar ratio of elements $Bi/P = 1.05$.

In Fig. 3, SEM images of the various particles of TiO_2 , ZnO, and Bi_2O_3 allow a comparative analysis of crystallites dimensions and morphologies.

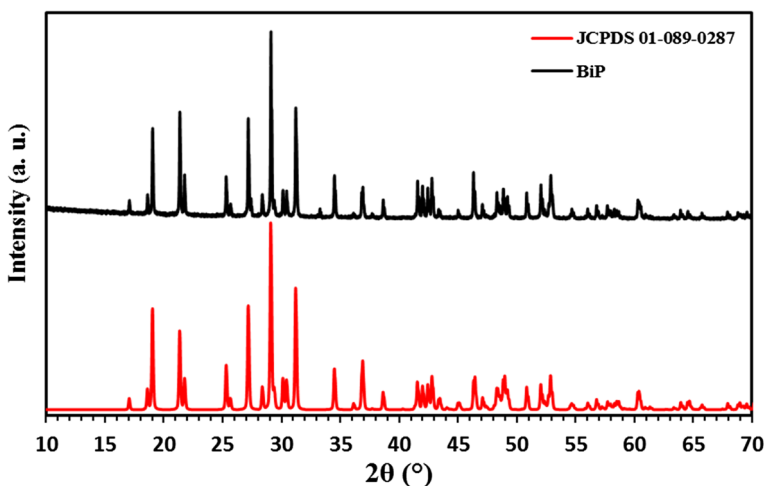


Fig. 1 XRD pattern of monoclinic $BiPO_4$ (space group $P2_1/n$)

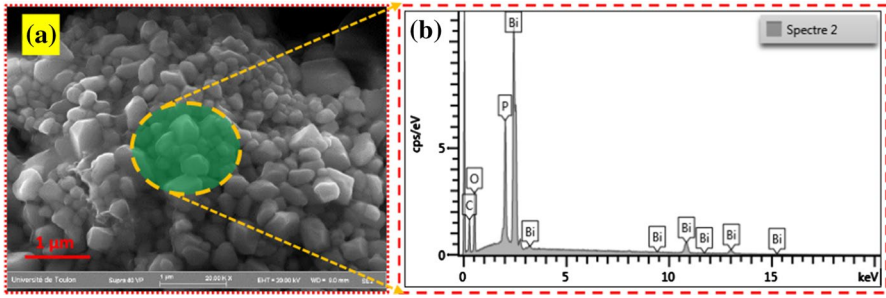


Fig. 2 a SEM images and b EDX spectrum of bismuth phosphate BiPO_4 treated at $500\text{ }^\circ\text{C}$

Table 1 EDX results on various spots on the BiPO_4 powder

	Percentage At. %			
	Zone 1	Zone 2	Zone 3	Average
Phosphorus	49.87	47.72	48.37	48.70
Bismuth	50.13	52.28	51.63	51.34

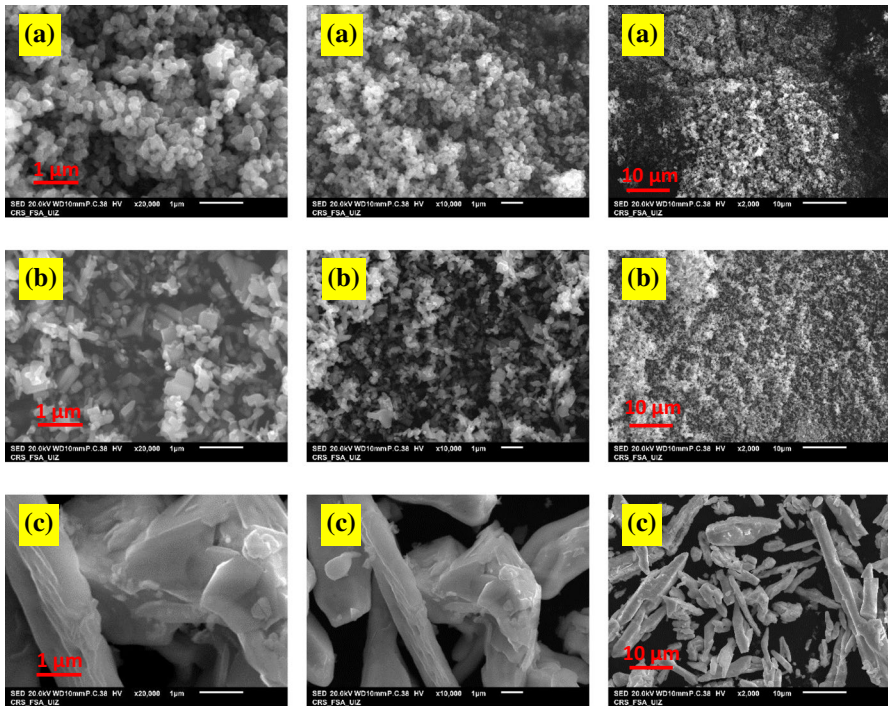


Fig. 3 SEM images of a TiO_2 , b ZnO and c Bi_2O_3

Figure 2a shows that the BiPO_4 material consists of submicronic grains characterized by regular shapes with presence of facets indicating a high level of crystallization. Figure 3 allow comparing the different crystallite sizes of this BiP material (Fig. 2) and the three standard compounds TiO_2 , ZnO , and Bi_2O_3 .

In Fig. 4, the distributions of particles sizes of BiP, TiO_2 , ZnO , and Bi_2O_3 are represented. The linear dimensions D of these particles range between 200 and 300 nm ($\langle D_{\text{BiP}} \rangle = 250 (\pm 50)$ nm) for BiPO_4 (Fig. 4a). For TiO_2 and ZnO , the SEM images (Fig. 4b, c) show that the powders are characterized by smaller sizes, with an average of $\langle D_{\text{TiO}_2} \rangle = 110 (\pm 10)$ nm (Fig. 4b) and $\langle D_{\text{ZnO}} \rangle = 145 (\pm 45)$ nm (Fig. 4c), for TiO_2 and ZnO , respectively.

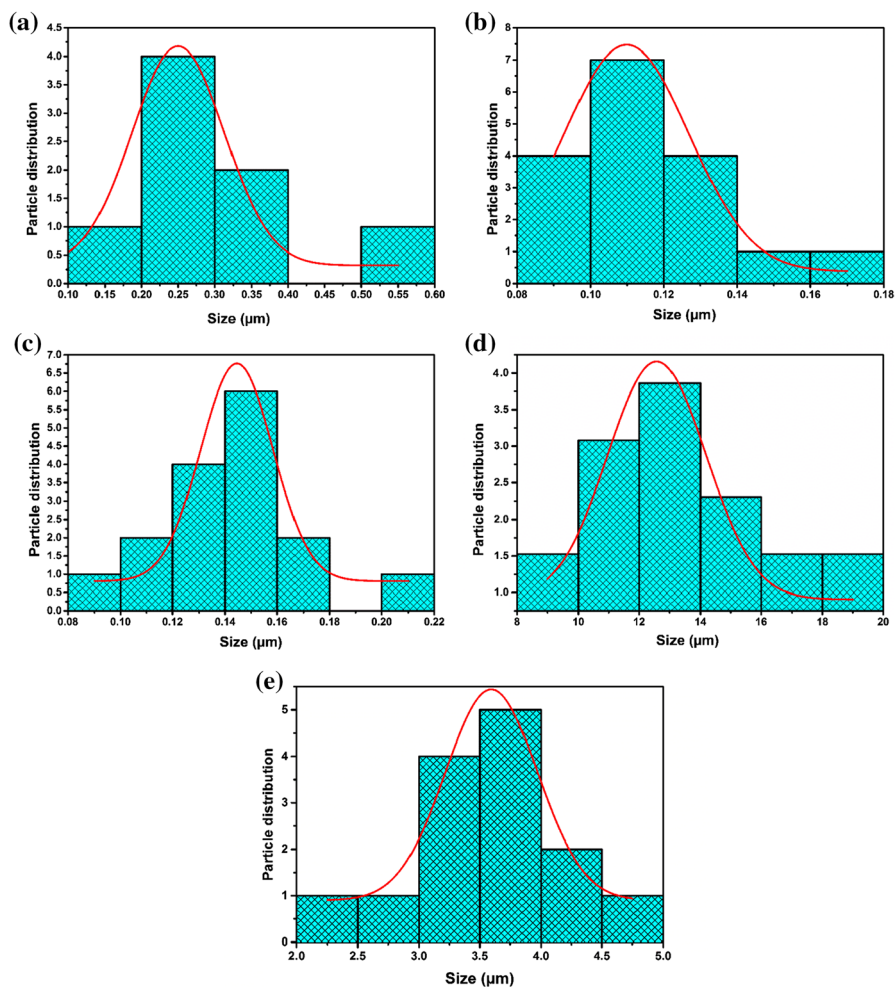


Fig. 4 Distributions of particle sizes of **a** BiP, **b** TiO_2 , **c** ZnO , **d** stick length and **e** stick width of Bi_2O_3 photocatalysts

In the case of Bi_2O_3 powder, the SEM images show the presence of large particles in form of elongated sticks with lengths of $\langle D_{\text{LBi}} \rangle = 12.5 (\pm 0.5) \mu\text{m}$ (Fig. 4d) and widths of $\langle D_{\text{WBi}} \rangle = 3.6 (\pm 0.6) \mu\text{m}$ (Fig. 4e).

From these SEM observations, a qualitative classification of specific surface areas by increasing values can be proposed (considering the different decreasing values of average sizes): $\text{Bi}_2\text{O}_3 < \text{BiP} < \text{ZnO} < \text{TiO}_2$.

Vibrational study by Raman spectroscopy

The Raman spectrum of the prepared BiP phase is represented in Fig. 5. It shows the presence of vibrational bands characteristic of bismuth phosphate [49, 50]. The isolated PO_4 group has a T_d symmetry with nine internal modes which can be represented as:

$$T_{\text{vib}} = A_1 + E + 2F_2 \quad (3)$$

The representation E is doubly degenerated and F_2 is triply degenerated. The mode belonging to the A_1 representation and one of the triply degenerated modes F_2 are generally ascribed to the symmetrical (ν_1) and asymmetrical (ν_3) P–O stretching vibrations of the PO_4 groups, respectively. The other modes F_2 and mode E correspond to O–P–O flexions ν_2 and ν_4 , respectively [51, 52]. In Table 2, the experimental wavenumbers 1039, 969, 597 and 461 cm^{-1} can be assigned to the ν_3 (asym. stretching), ν_1 (sym. stretching), ν_4 and ν_2 (bending) modes, respectively. Lattice modes in the 150–400 cm^{-1} range are generally attributed to vibrations involving the movements of cations and tetrahedron units (see Table 2). The well-defined profiles of Raman bands confirm the high degree of crystallization of the BiP powder.

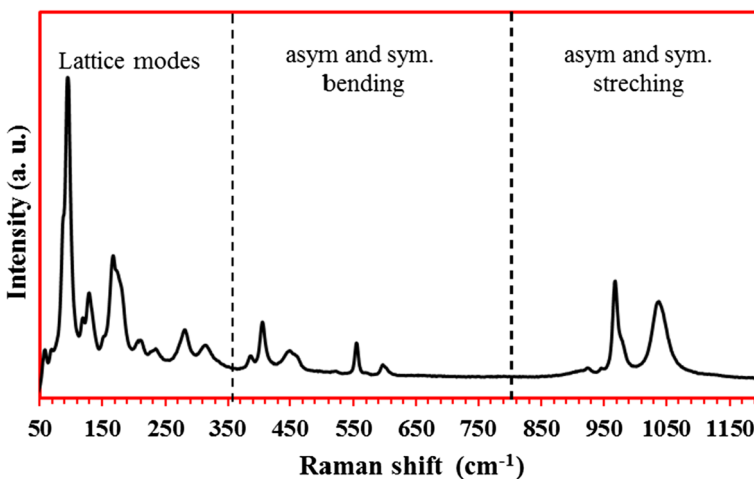


Fig. 5 Raman spectrum of BiPO_4 sample

Table 2 Raman spectroscopy data and assignments of vibration bands for the BiP monoclinic phase P2₁/n

Raman data for monoclinic BiPO ₄ (P2 ₁ /n)	
Wavenumbers in cm ⁻¹	Assignments
1039	ν_3 : PO ₄ Asym. Stretching
–	–
969	ν_1 : PO ₄ Sym. Stretching
924	–
597	ν_4 : Bending modes of PO ₄
556	–
461	ν_2 : Bending modes of PO ₄
388	–
281	Bending modes of O–Bi–O
169	Stretching vibrations of Bi–O

Photocatalytic degradation of RhB

RhB adsorption and photolysis tests on BiPO₄

To correctly analyze the kinetics of photodegradation reactions, it is essential to separate the adsorption phenomena from the degradation phenomena on the surfaces of the photocatalysts. For this, we followed the evolution of this process for a period of 5 h and under the same experimental conditions of photocatalysis.

Figure SI.2a shows the absorption spectrum of RhB in presence of BiP. It is noted that the decrease of the maximum of the RhB absorption band does not exceed 4.1% after 5 h, which shows that the adsorption of RhB on BiPO₄ particles is extremely weak.

In the same sense, to evidence the photocatalytic activity of our photocatalyst, it was essential to carry out the test of direct photolysis of rhodamine B under the same operating conditions of photocatalysis. To this end, we studied the effect of UV light on the degradation of pollutant in the absence of any photocatalyst. This study was carried out using a solution with an initial concentration of 5 mg L⁻¹ under UV irradiation. Figure SI.2b shows that, in the absence of photocatalyst, only a degradation of 2% of RhB is obtained after 12 min of irradiation under UV light. This result agrees with the literature results on the degradation of RhB by direct photolysis, using UV irradiation at 254 nm.

Photocatalytic performance of monoclinic BiP

To well characterize the photocatalytic performance of these BiP particles, we carried out a series of photodegradation experiments of RhB, using a fixed mass of BiP, TiO₂, ZnO, and Bi₂O₃ particles. It should be noted that the energy of the irradiation source used in this work ($E=4.87$ eV) was greater than the gap

energies of these photocatalysts: BiPO_4 ($E_g = 3.8$ eV) [19], TiO_2 ($E_g = 3.2$ eV) [53], ZnO ($E_g = 3.3\text{--}3.4$ eV) [54] and Bi_2O_3 ($E_g = 2.6\text{--}2.8$ eV) [55–57].

The decrease of the maximum absorbance intensity of RhB at $\lambda_{\text{max}} = 554$ nm was the main factor to evaluate the photocatalytic activity of each sample.

Figure 6 show that, under UV irradiation, the RhB absorption band intensities decrease with the irradiation time, in the presence of the photocatalysts BiPO_4 , TiO_2 , ZnO , and Bi_2O_3 . The positions of these absorption bands have shifted from 554 nm during irradiation. These shifts of absorption bands are mainly due to the formation of the degradation intermediates of RhB with maximum absorption different from the RhB molecule.

Figure 7a shows the variations of the ratio $C(t)/C_0$ as a function of time for the different photocatalysts. After 12 min of UV–visible irradiation (UV source: 254 nm), the photocatalytic efficiencies determined from the ratio $C(t)/C_0$, for the BiPO_4 , TiO_2 , ZnO and Bi_2O_3 , reach the values of 96%, 81.6%, 76.2% and 23.1%, respectively. As the effect of photolysis was previously shown to be very weak, it should be noted that these efficiencies would result from the sole effect of

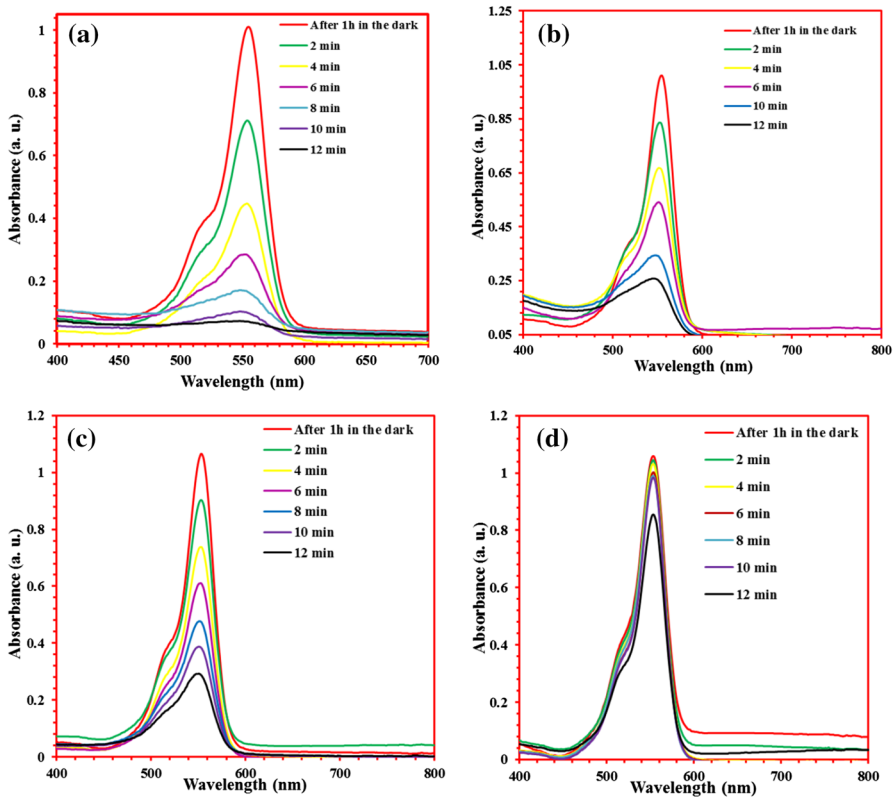


Fig. 6 UV–vis absorption bands as a function of time irradiation of a solution containing 100 mg of photocatalyst and 5 ppm of RhB, **a** BiPO_4 , **b** TiO_2 , **c** ZnO , and **d** Bi_2O_3

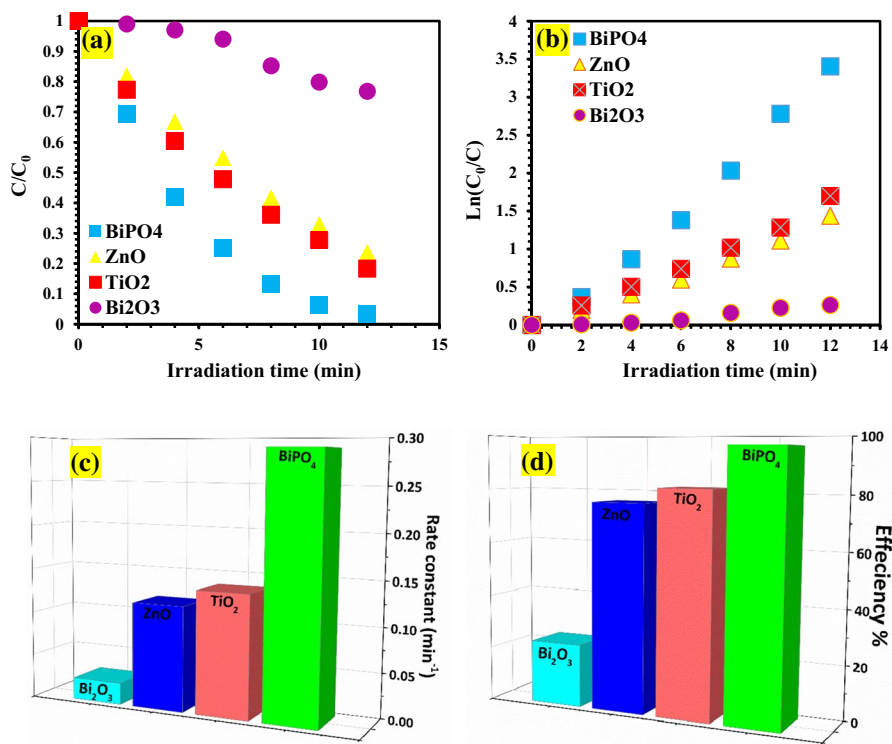


Fig. 7 **a** Degradation efficiencies of the powders, **b** pseudo-first-order kinetics of the photocatalysts, **c** Evolution of the rate constant k as a function of photocatalysts, and **d** Efficiency of degradation after irradiation time of 12 min, for different photocatalysts

photocatalysis. The degradation kinetics was evaluated by determining rate constants and half-life times. The results obtained for the photodegradation of rhodamine B were adjusted to the Langmuir–Hinshelwood first-order kinetics (Fig. 7b).

Table 3 Photocatalytic efficiencies, pseudo-first-order rate constants (k), half-life times ($t_{1/2}$), and linear regressions (R) for BiP, TiO₂, ZnO, and Bi₂O₃ photocatalysts in presence of RhB under UV–visible irradiation (254 nm)

Photocatalytic parameters	Catalysts			
	BiPO ₄	TiO ₂	ZnO	Bi ₂ O ₃
Mass of photocatalyst (in mg)	100	100	100	100
Efficiency after 12 min	96.6	81.6	76.2	23.1
Crystallite size D in nm	250	110	145	12,500*3620
k (min ⁻¹)	0.2893	0.1368	0.1180	0.0241
$T_{1/2}$ (min)	2.39	5.06	5.87	28.76
R (correlation)	0.9891	0.9922	0.9921	0.9293

Table 3 brings together the various characteristics of each photocatalyst: the photodegradation efficiencies after 12 min of irradiation, the apparent rate constants k (in min^{-1}), the half-life times ($t_{1/2}$) and linear regressions (R). An extremely high performance of the BiP particles is thus evidenced, in comparison with those of the other photocatalysts.

Figure 7c, d report the rate constants k and the degradation efficiency $\mathbf{DE(t)}$ after 12 min for all photocatalysts, respectively. These diagrams thus highlight the high performance of the BiP photocatalysts compared to the lower performances of the TiO_2 , ZnO, and Bi_2O_3 photocatalysts [48].

The study of the effects of scavengers in the photodegradation of RhB showed that holes (h^+) and superoxide radicals ($\text{O}_2^{\cdot-}$) were the dominating active species on the surface of the BiPO_4 photocatalyst [48].

LC-UV/Vis-MS studies for product analysis

The chromatogram of the standard RhB solution at a concentration of 5 ppm is presented in Fig. 8. This chromatogram shows that, in addition to the characteristic peak of RhB molecules ($\text{tr}=21.4$ min) [58], two peaks ($\text{tr}=2.4$ and 2.7 min) appear which are due to impurities from the water used as the mobile phase with methanol.

The HPLC spectrum was then used to monitor the photodegradation of RhB and analyze the appearance and disappearance of the photooxidation intermediates. Figure 9 shows the HPLC spectral diagrams of RhB and the degradation products in the presence of BiP-500 °C photocatalyst. From the analysis of these spectra, RhB was rapidly transformed into its intermediates characterized by well-defined wavelengths. Three main components corresponding to maximum

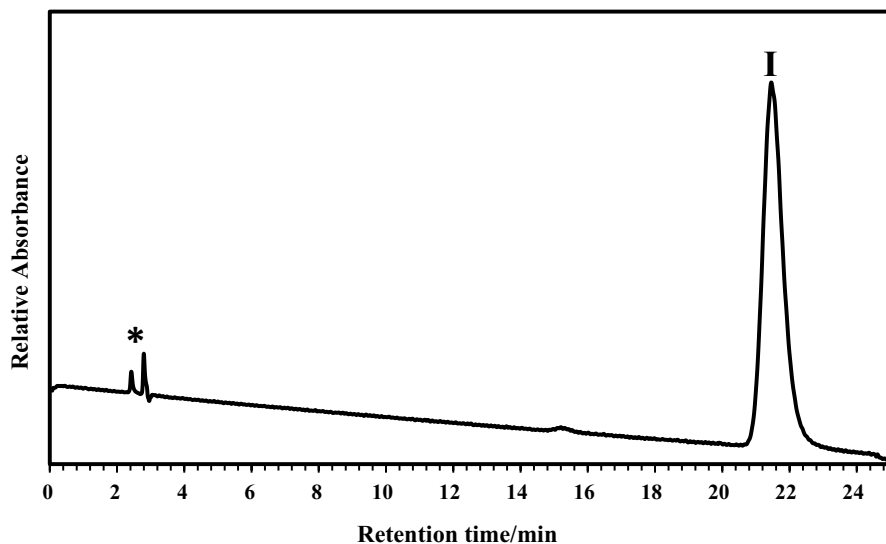


Fig. 8 Typical chromatogram obtained at 552 nm for a standard solution containing 5 mg mL^{-1} RhB (peak I). * is that of an impurity in the mobile phase

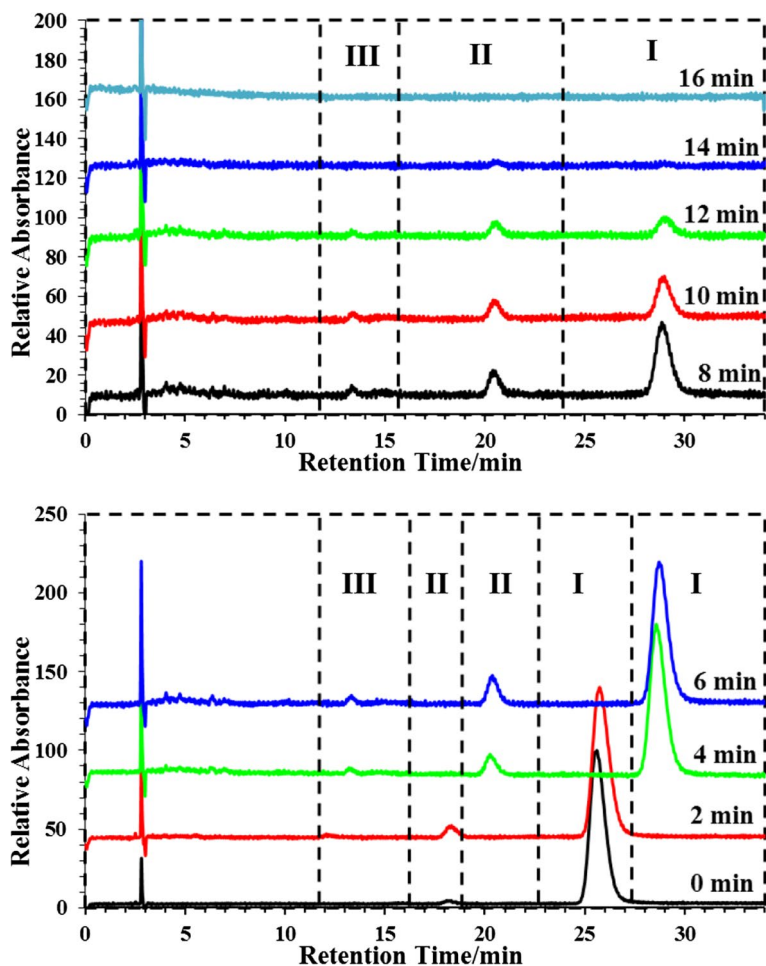


Fig. 9 HPLC spectra of RhB and its photodegradation intermediates in the presence of BiP under UV light irradiation. The detected solution in the HPLC measurement was checked by UV–VIS detector

absorptions at 552 nm (product I, retention time: 25.6 min), 538 nm (product II, retention time: 18.1 min), and 547 nm (product III, retention time: 12 min) have been detected [59]. These first retention times of the intermediates are not fixed, the HPLC spectra showing a systematic shift towards the large retention times as a function of UV irradiation time during the photocatalytic degradation (Table 4). The degradation products of RhB were also analyzed by the LC–MS technique for the identification and confirmation of intermediates during the elimination process. The ESI mass spectra in positive ion mode are presented in Figure SI.1. The molecular structure of these intermediates was then identified by LC–MS, HPLC combining with the UV VIS spectra. The main intermediates corresponding to the m/z values are listed in Table 5.

Table 4 Retention time of photodegradation intermediates of RhB as a function of the irradiation time

Irradiation time (min)	Retention time (min)		
	N-ethyl-N'-ethyl-rhodamine 110 (MMRh)	N,N-diethyl-N'-ethyl-rhodamine 110 (DMRh)	Rhodamine B (RhB)
0 min	–	18.0	25.6
2 min	12.0	18.3	25.7
4 min	13.1	20.2	25.7
6 min	13.3	20.3	28.5
8 min	13.3	20.4	28.8
10 min	13.3	20.4	28.9
12 min	13.3	20.6	28.9
14 min	–	20.6	–
16 min	–	–	–

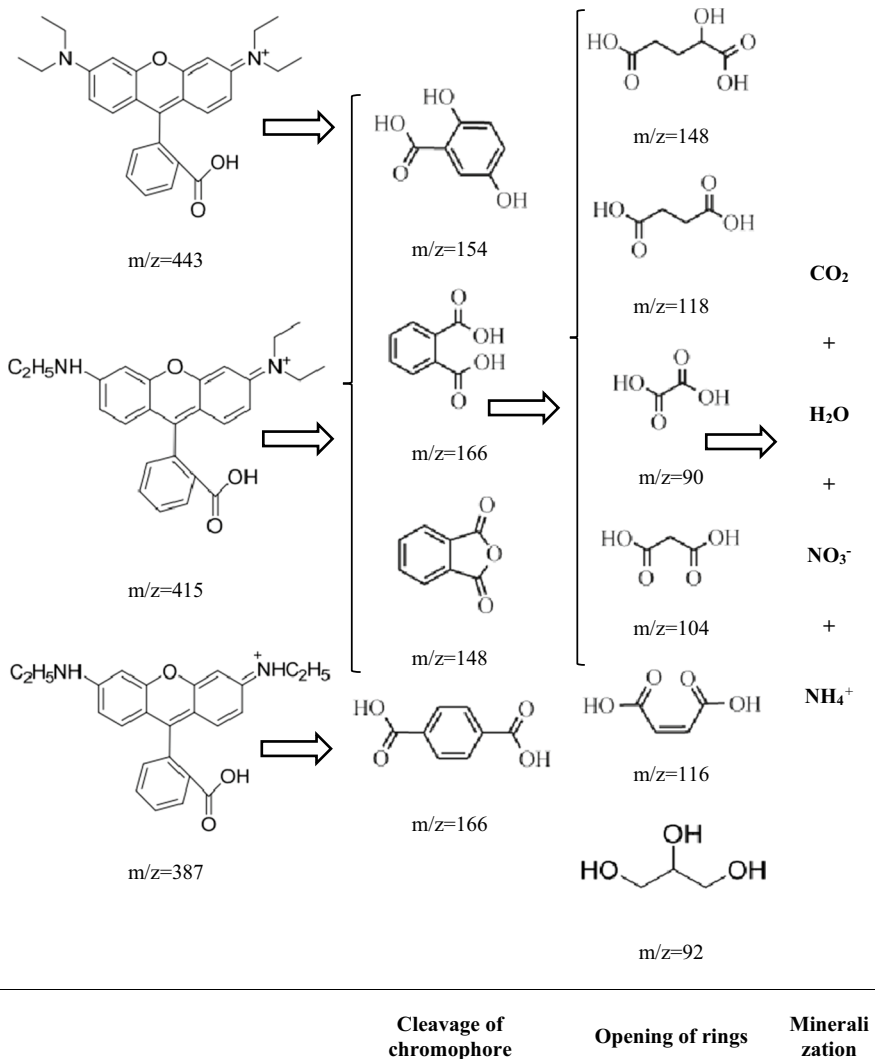
Table 5 Identification of photodegradation intermediates of RhB by HPLC and LC–MS (positive ion mode ESI mass spectra)

HPLC peaks	Absorption maximum (nm)	Corresponding intermediaries of RhB	m/z	Assigned substrates
III	547	N-ethyl-N'-ethyl-rhodamine 110 (MMRh)	387.1	MMRh ⁺
			409.1	MMRh-Na ⁺
II	538	N,N-diethyl-N'-ethyl-rhodamine 110 (DMRh)	415.1	DMRh ⁺
			437.1	DMRh-Na ⁺
I	552	Rhodamine B (RhB)	443.1	RhB ⁺
			465.1	RhB-Na ⁺

The identification of the intermediates confirmed that the deethylation process occurred in the presence of the BiP photocatalysts and under UV irradiation for 16 min. More precisely, the starting molecule of RhB ($m/z=443$) has lost the ethyl groups step by step to transform into the products such as N,N-diethyl-N'-ethyl-rhodamine 110 (DMRh, $m/z=415$), and N-ethyl-N'-ethyl-rhodamine 110 (MMRh, $m/z=387$) and until the total disappearance of the three components after 16 min of irradiation.

Corresponding to the LC/MS and GC/MS identification, the possible photocatalytic degradation pathway of RhB in the presence of BiPO₄ can be proposed (Scheme 1). It is well-known that the RhB degradation occurs via two competitive processes [60]. One is stepwise N-deethylation, and the other is the destruction of the conjugated structure.

The resulting intermediates were further degraded sequentially by the cleavage of various bonds and eventually led to the formation of expected final product of photocatalytic degradation of RhB as phthalic acid ($m/z=166$), terephthalic acid



Scheme 1 Possible degradation pathway of RhB dye by BiP catalyst under UV light irradiation

($m/z = 166$)....etc. [61–63]. After the conjugated structure of RhB was degraded, two other processes, opening—ring and mineralization were following, and some organic acidic molecules were produced, which were mineralized to carbon dioxide, water, nitrate, and ammonium cation at the end.

Photoluminescence properties

The photoluminescence spectra of our BiP material are shown in Fig. 10, they were recorded in three different sample zones of the polycrystalline BiPO_4 material. The

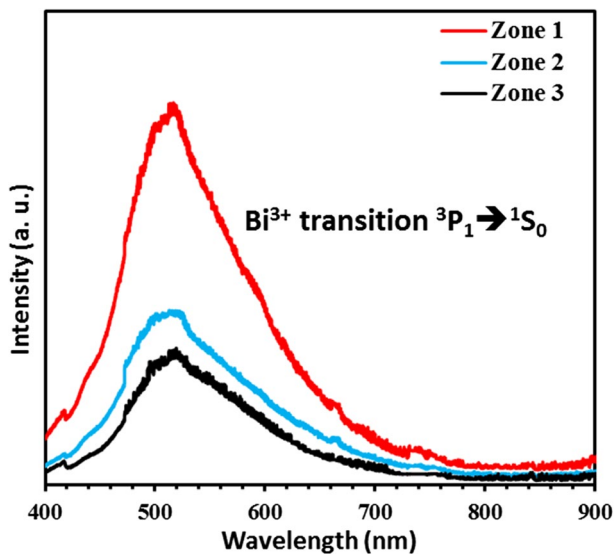


Fig. 10 Photoluminescence spectra under UV excitation (364 nm) of the BiP polycrystalline phase

emission spectra were processed using Labspec program. The broad emission bands observed in the range 500 to 600 nm in all zones present similar profiles with a maximum of 515 ± 20 nm. Literature results showed that, in the case of isolated Bi^{3+} in solid matrix, the allowed Bi^{3+} transition ${}^3\text{P}_1^1\text{S}_0$ was characterized by emission spectra with wavelengths close to 470 nm (2.6 eV). In the case of the study of BiPO_4 polymorphs, the Bi^{3+} emissions under excitation at 360 nm (3.4 eV) were observed at 450 nm (2.8 eV), for both hexagonal and monoclinic phases. Presently, a wide emission band (450–700 nm) is systematically observed: the emission profile can be decomposed into several emissions including at least three components (470, 510–520, and 600–680 nm). The emissions ranging from 500 to 700 nm are generally ascribed to surface defects. This was also the case in our previous work [15, 24] on BiPO_4 , where a similar large band was linked to the monoclinic structure with $\text{P2}_1/n$ space group and ascribed to transitions associated with the modifications of Bi^{3+} environments, due to the presence of oxygen vacancy defects $[\text{V}_\text{O}]^{q^\circ}$ (where q° is the positive electrical charge with $q=0, 1$ or 2) perturbing the PO_4 and BiO_8 structural groups of the monoclinic structure. Other defects could also be at the origin of this large band (Bi vacancies or interstitials).

Conclusion

In conclusion, the highly efficient photocatalytic performance of submicron monoclinic BiP particles synthesized via solid-state reactions is highlighted. These submicron particles' photocatalytic activity was found to be higher than that of TiO_2 and ZnO particles, characterized by smaller crystallite size, and higher than that of

large-scale commercial Bi_2O_3 photocatalysts. This clearly shows that this high performance is not due to size effects or high specific surface area, but rather due to the nature of surface defects. The photoluminescence analysis has shown strong emission in a broad color range from blue to red, the composition of which is due to surface defects, including oxygen vacancies and changes in the Bi^{3+} environment. According to all these results, the BiPO_4 submicronic powder with monoclinic M_1 form, prepared by solid-state reaction technique, shows both significant photocatalytic and photoluminescent properties and may be useful for environmental applications.

Supplementary Information The online version contains supplementary material available at <https://doi.org/10.1007/s11164-022-04762-1>.

Acknowledgements Financial support was obtained from CAMPUS FRANCE (PHC TOUBKAL 2018, French-Morocco bilateral program, Grant Number: 38999WE) and from PPR project financed by the CNRST under number PPR/2015/32.

Declarations

Conflict of interest The authors declare that they have no conflict of interest.

References

1. P. Dumrongrojthanath, T. Saksoong, P. Patiphatpanya, A. Phuruangrat, S. Thongtem, T. Thongtem, *Res. Chem. Intermed.* **45**, 2301 (2019)
2. X. Zhou, X. Wang, J. Li, X. Zhang, *Res. Chem. Intermed.* **47**, 1519 (2021)
3. C. Chen, L. Xun, P. Zhang, J. Zhang, B. Tian, *Res. Chem. Intermed.* **45**, 3513 (2019)
4. Y. Ma, J. Chen, Y. Wang, Y. Zhao, G. Zhang, T. Sun, *Res. Chem. Intermed.* **47**, 997 (2020)
5. K. Zhong, J. Su, *Res. Chem. Intermed.* **45**, 1207 (2018)
6. E. Amaterz, A. Bouddouch, A. Tara, A. Taoufyq, B. Bakiz, A. Benlhachemi, O. Jbara, *Opt. Mater. (Amst)*. **109**, 110268 (2020)
7. R. Haounati, A. El Guerdaoui, H. Ouachtak, R. El Haouti, A. Bouddouch, N. Hafid, B. Bakiz, D.M.F. Santos, M. Labd Taha, A. Jada, A. Ait Addi, *Sep. Purif. Technol.* **277**, 119399 (2021)
8. M. Ge, *Chin. J. Catal.* **35**, 1410 (2014)
9. H. Lin, H. Ye, B. Xu, J. Cao, S. Chen, *Catal. Commun.* **37**, 55 (2013)
10. C. Pan, D. Li, X. Ma, Y. Chen, Y. Zhu, *Catal. Sci. Technol.* **1**, 1399 (2011)
11. E. Amaterz, A. Tara, A. Bouddouch, A. Taoufyq, B. Bakiz, A. Benlhachemi, O. Jbara, *Rev. Environ. Sci. Biotechnol.* **19**, 843 (2020)
12. E. Amaterz, A. Bouddouch, A. Chennah, A. Tara, A. Taoufyq, B. Bakiz, F. Lazar, A. Benlhachemi, L. Bazzi, and O. Jbara, in *Mater. Today Proc.* (Elsevier Ltd, 2020), pp. 45–47.
13. B. Cao, P. Dong, S. Cao, Y. Wang, *J. Am. Ceram. Soc.* **96**, 544 (2013)
14. L.-W. Cheng, J.-C. Tsai, T.-Y. Huang, C.-W. Huang, B. Unnikrishnan, Y.-W. Lin, *Mater. Res. Express* **1**, 025023 (2014)
15. A. Bouddouch, E. Amaterz, B. Bakiz, A. Taoufyq, F. Guinneton, S. Villain, J.R. Gavarri, J.C. Valmalette, A. Benlhachemi, *Nanotechnol. Environ. Eng.* **6**, 1 (2021)
16. L. Li, J. Xu, C. Guo, Y. Zhang, *Front. Environ. Sci. Eng.* **7**, 382 (2013)
17. C. Chi, J. Pan, M. You, Z. Dong, W. Zhao, C. Song, Y. Zheng, C. Li, *J. Phys. Chem. Solids* **114**, 173 (2018)
18. R.C.L. Mooney-Slater, *Zeitschrift Fur Krist. - New Cryst. Struct.* **117**, 371 (1962)
19. C. Pan, Y. Zhu, *Environ. Sci. Technol.* **44**, 5570 (2010)
20. H. Xu, Y. Xu, H. Li, J. Xia, J. Xiong, S. Yin, C. Huang, H. Wan, *Dalt. Trans.* **41**, 3387 (2012)

21. A. Bouddouch, E. Amaterz, B. Bakiz, A. Taoufyq, F. Guinneton, S. Villain, J. C. Valmalette, J. R. Gavarri, and A. Benlhachemi, *Optik (Stuttg)* **238**, 166683 (2021)
22. A. Hallaoui, A. Taoufyq, M. Arab, B. Bakiz, A. Benlhachemi, L. Bazzi, S. Villain, J.C. Valmalette, F. Guinneton, J.R. Gavarri, *J. Solid State Chem.* **227**, 186 (2015)
23. M. Khachane, A. Bouddouch, B. Bakiz, A. Benlhachemi, Y. Kadmi, *Int. J. Environ. Sci. Technol.* **2021**, 1 (2021)
24. A. Bouddouch, E. Amaterz, B. Bakiz, A. Taoufyq, F. Guinneton, S. Villain, J. Gavarri, M. Ezahri, J. Valmalette, A. Benlhachemi, *Water Environ. Res.* **92**, 1874 (2020)
25. B.J. Jin, S.H. Bae, S.Y. Lee, S. Im, *Mater. Sci. Eng. B* **71**, 301 (2000)
26. J. Liao, W. Cui, J. Li, J. Sheng, H. Wang, X. Dong, P. Chen, G. Jiang, Z. Wang, F. Dong, *Chem. Eng. J.* **379**, 122282 (2020)
27. H.K. Yadav, K. Sreenivas, V. Gupta, S.P. Singh, R.S. Katiyar, *J. Mater. Res.* **22**, 2404 (2007)
28. H. Yuan, M. Xu, K. Luo, W. Hu, *Ceram. Int.* **45**, 16694 (2019)
29. C. Pan, J. Xu, Y. Chen, Y. Zhu, *Appl. Catal. B Environ.* **115–116**, 314 (2012)
30. T. Fei, L. Yu, Z. Liu, Y. Song, F. Xu, Z. Mo, C. Liu, J. Deng, H. Ji, M. Cheng, Y. Lei, H. Xu, H. Li, *J. Colloid Interface Sci.* **557**, 498 (2019)
31. Y. Zhu, Y. Wang, Q. Ling, Y. Zhu, *Appl. Catal. B Environ.* **200**, 222 (2017)
32. Y. Naciri, A. Bouddouch, B. Bakiz, A. Taoufyq, M. Ezahri, and A. Benlhachemi, in *Mater. Today Proc.* (Elsevier Ltd, 2020), pp. 48–51.
33. S. Huang, G. Wang, J. Liu, C. Du, Y. Su, *ChemCatChem* **12**, 4431 (2020)
34. A.S. Morshedy, H.R. Ali, A.A. Nada, A.M. Rabie, H.H. El-Maghrabi, *Environ. Technol. Innov.* **21**, 101206 (2021)
35. S. Iqbal, A. Bahadur, M. Javed, O. Hakami, R.M. Irfan, Z. Ahmad, A. AlObaid, M.M. Al-Anazy, H.B. Baghdadi, H.S.M. Abd-Rabboh, T.I. Al-Muhimeed, G. Liu, M. Nawaz, *Mater. Sci. Eng. B* **272**, 115320 (2021)
36. L. Song, Z. Chen, T. Li, S. Zhang, *Mater. Chem. Phys.* **186**, 271 (2017)
37. S. Obregón, G. Colón, *Appl. Catal. B Environ.* **158–159**, 242 (2014)
38. Y. Yang, B. Liu, Y. Zhang, X. Lv, L. Wei, X. Wang, *Superlattices Microstruct.* **90**, 227 (2016)
39. G. Muruganandam, N. Mala, S. Pandiarajan, N. Srinivasan, R. Ramya, E. Sindhuja, K. Ravichandran, *J. Mater. Sci. Mater. Electron.* **28**, 18228 (2017)
40. M. Srinivas, *Mater. Sci. Eng. B* **270**, 115222 (2021)
41. I. Ellouzi, A. Bouddouch, B. Bakiz, A. Benlhachemi, H. Abou Oualid, *Chem. Phys. Lett.* **770**, 138456 (2021)
42. N. Wang, L. Lei, X.M. Zhang, Y.H. Tsang, Y. Chen, H.L.W. Chan, *Microelectron. Eng.* **88**, 2797 (2011)
43. A. Soto-Arreola, A.M. Huerta-Flores, J.M. Mora-Hernández, L.M. Torres-Martínez, *J. Photochem. Photobiol. A Chem.* **357**, 20 (2018)
44. R. Saravanan, V.K. Gupta, V. Narayanan, A. Stephen, *J. Mol. Liq.* **181**, 133 (2013)
45. Y. Wang, X. Li, N. Wang, X. Quan, Y. Chen, *Sep. Purif. Technol.* **62**, 727 (2008)
46. A. Bouddouch, E. Amaterz, R. Haounati, Y. Naciri, A. Taoufyq, B. Bakiz, F. Guinneton, S. Villain, J.-R. Gavarri, A. Benlhachemi, *Mater. Today Proc.* **3**, 2 (2010)
47. A. Bouddouch, E. Amaterz, A. Taoufyq, B. Bakiz, F. Guinneton, S. Villain, J. Valmalette, J.R. Gavarri, A. Benlhachemi, *Mater. Today Proc.* **27**, 3139 (2020)
48. A. Bouddouch, E. Amaterz, B. Bakiz, A. Taoufyq, F. Guinneton, S. Villain, J.-R. Gavarri, J.-C. Valmalette, A. Benlhachemi, *Minerals* **11**, 1007 (2021)
49. M. Zhao, L. Li, L. Yang, J. Zheng, G. Li, *CrystEngComm* **15**, 609 (2013)
50. M.E. Poloznikova, V.V. Fomichev, *Russ. Chem. Rev.* **63**, 399 (1994)
51. E.N. Silva, A.P. Ayala, I. Guedes, C.W.A. Paschoal, R.L. Moreira, C.-K. Loong, L.A. Boatner, *Opt. Mater. (Amst)*. **29**, 224 (2006)
52. J. Heuser, A.A. Bukaemskiy, S. Neumeier, A. Neumann, D. Bosbach, *Prog. Nucl. Energy* **72**, 149 (2014)
53. D. Chen, A.K. Ray, *Appl. Catal. B Environ.* **23**, 143 (1999)
54. H.G. Chen, J.L. Shi, H.R. Chen, J.N. Yan, Y.S. Li, Z.L. Hua, Y. Yang, D.S. Yan, *Opt. Mater. (Amst)*. **25**, 79 (2004)
55. S. Shamaila, A.K.L. Sajjad, F. Chen, J. Zhang, *Appl. Catal. B Environ.* **94**, 272 (2010)
56. S.Y. Chai, Y.J. Kim, M.H. Jung, A.K. Chakraborty, D. Jung, W.I. Lee, *J. Catal.* **262**, 144 (2009)
57. A. Hameed, T. Montini, V. Gombac, P. Fornasiero, *J. Am. Chem. Soc.* **130**, 9658 (2008)
58. L. Gagliardi, D. De Orsi, G. Cavazzutti, G. Multari, D. Tonelli, *Chromatographia* **43**, 76 (1996)

59. F. Chen, J. Zhao, H. Hidaka, *Int. J. Photoenergy* **5**, 209 (2003)
60. J. Li, X. Zhang, Z. Ai, F. Jia, L. Zhang, J. Lin, *J. Phys. Chem. C* **111**, 6832 (2007)
61. T.S. Natarajan, K. Natarajan, H.C. Bajaj, R.J. Tayade, *J. Nanoparticle Res.* **15**, 1 (2013)
62. S. Dixit, S.K. Khanna, M. Das, *J. AOAC Int.* **94**, 1874 (2011)
63. T. Rasheed, M. Bilal, H.M.N. Iqbal, S.Z.H. Shah, H. Hu, X. Zhang, Y. Zhou, *Environ. Technol.* **39**, 1533 (2018)

Publisher's Note Springer Nature remains neutral with regard to jurisdictional claims in published maps and institutional affiliations.